DEVELOPMENT OF IMAGING METHODS TO QUANTIFY THE LAMINAR MICROSTRUCTURE IN RAT HEARTS

A Thesis

by

KRISTEN KAY HUDSON

Submitted to the Office of Graduate Studies of
Texas A&M University
in partial fulfillment of the requirements for the degree of

MASTER OF SCIENCE

August 2004

Major Subject: Biomedical Engineering

DEVELOPMENT OF IMAGING METHODS TO QUANTIFY THE LAMINAR MICROSTRUCTURE IN RAT HEARTS

A Thesis

by

KRISTEN KAY HUDSON

Submitted to Texas A&M University
in partial fulfillment of the requirements
for the degree of

MASTER OF SCIENCE

Approved as to style and content by:

John Criscione (Chair of Committee)	Gerard Coté (Member)
Kelly Credille (Member)	William Hyman (Head of Department)

August 2004

Major Subject: Biomedical Engineering

ABSTRACT

Development of Imaging Methods to Quantify the Laminar Microstructure in Rat Hearts. (August 2004)

Kristen Kay Hudson, B.S., Texas A&M University

Chair of Advisory Committee: Dr. John Criscione

The way in which the myocardium responds to its mechanical environment must be understood in order to develop reasonable treatments for congestive heart failure. The first step toward this understanding is to characterize and quantify the cardiac microstructure in healthy and diseased hearts. Myocardium has a laminar architecture made up of myolaminae, which are sheets of myocytes surrounded by a collagen weave. By enhancing the contrast between the myocytes and the surrounding collagen, the myocardium can be investigated and its laminar structure can be quantified. Many of the techniques that have been used to view the microstructure of the heart require the use of toxic or caustic chemicals for fixation or staining. An efficient imaging method that uses polarization microscopy and enhances the contrast between the collagen and myocytes while minimizing the use of harmful chemicals was developed in this research. Collagen is birefringent; therefore its visibility should be enhanced through polarization microscopy and image processing. The sheet angles were viewed directly by cutting slices of a rat septum perpendicular to the fiber angle. Images of different polarization combinations were taken and a region of interest was selected on the sample. Image processing techniques were used to reduce the intensity variation on the images and account for the variable gain of the camera. The contrast between the collagen and myocytes was enhanced by comparing adjusted images to the background and looking at a single image this comparison produced. Although the contrast was enhanced, the embedding media reduced the collagen signal and the enhancement was not as striking as expected.

ACKNOWLEDGEMENTS

I would like to thank Dr. Gerard Coté, Justin Baba, and Mustafa Chowdhury of the Optical Biosensing Laboratory at Texas A&M University for their help in acquiring preliminary data for this thesis. I would also like to thank Dr. John Criscione and Emily Jetton for their help on all aspects of this project. This research was funded by the American Heart Association grant #0265133Y awarded to Dr. John Criscione.

TABLE OF CONTENTS

Page

LIST OF FIGURES

FIGURE Page

INTRODUCTION

Motivation and Rationale

Heart disease occurs in almost every American family, and one particular condition, congestive heart failure (CHF), presently afflicts 5 million Americans (American Heart Association, 2003). As with most medical conditions, treatments for this disease will improve as knowledge of the pathophysiology progresses. To understand how the myocardium grows and remodels in response to its mechanical environment, the cardiac microstructure must first be characterized. Many histological investigations of myocardium focus on its main constituents: collagen and myocytes. Collagen is the protein that makes up much of the extracellular matrix (ECM). Myocytes are the cardiac muscle cells responsible for contraction. In order to relate cardiac microstructure to cardiac function, it is more beneficial to investigate the myocardium as a composite structure instead of focusing on its constituents.

The fundamental structural unit of the myocardium is the myolamina, which is a sheet of myocytes surrounded by a collagen weave (LeGrice et al., 1995a). The myolaminae branch and connect to adjacent sheets of cells via long fine collagen bundles (Caulfield and Borg, 1979). Gaps, or cleavage planes, are present between the myolaminae. These gaps appear to be important for the substantial changes in the size of the ventricle and thickness of the wall that the heart undergoes during contraction and relaxation because they allow the sheets to slide along one another.

The functional significance of the laminar organization of the heart appears to be that it allows myocardium to undergo large shearing deformation without developing large shear stress. In the process of ejecting most (>60%) of the ventricular contents, myocardium undergoes a substantial, finite deformation or distortion. According to the data from Costa et al., the outer part of the left ventricle wall experiences much less shear deformation than the inner part of the wall (Costa et al., 1999). If the laminar structure is directly modulated by shear, then it stands to reason that a transmural

---

This thesis is modeled after the Journal of Biomechanics.

variation in laminar organization will exist. The primary objective of this research is to develop imaging methods that will clearly reveal the microstructure. The transmural variation in the structure of the rat heart can then be described and quantified.

Our interest lies with the pathophysiology of congestive heart failure, and in order to better treat this condition, the way in which the myocardium grows and remodels in response to mechanical stimuli needs to be understood. The first step toward this understanding is quantifying the laminar microstructure in both healthy and diseased hearts. Many of the techniques that have been used to view myocardium require fixing or staining the tissue with toxic or caustic chemicals in order to enhance the contrast between collagen and myocytes (Emery and Omens, 1997; Junqueira et al., 1979; Weber et al., 1994; Whittaker et al., 1989, 1994; Young et al., 1998). Picrosirius red (PSR) is a stain that is specific for collagen when used in conjunction with polarized light, however, PSR gives the best results when the tissue is fixed in Bouin's solution (Young et al., 1998). Bouin's solution contains formaldehyde, acetic acid, and picric acid, all of which can have irritating effects on the eyes, skin, mucous membranes, respiratory system, central nervous system, and kidneys (Ricca Chemical Company, 2001). Picric acid is also an ingredient in the picrosirius red stain. In addition to causing irritation to the systems previously mentioned, it is highly explosive when dry (J.T. Baker, 2003). By eliminating the need for several of these harmful chemicals, the techniques used to image myocardium can be simplified and made safer.

Congestive Heart Failure

In congestive heart failure (CHF), the heart is unable to pump enough blood to meet the requirements of the body, or it is only able to do so as a result of an abnormally high filling pressure or diastolic volume. The heart tries to maintain pressure and perfusion by several adaptive mechanisms, but often the compensated heart eventually deteriorates into failure due to some acute disturbance. CHF can be described in a number of ways: systolic or diastolic, right-sided or left-sided, and forward or backward. Systolic dysfunction is more common and results in impaired contractility of the

ventricle. An inadequate amount of blood is ejected when the ventricle contracts. Diastolic dysfunction is characterized by the inability of a ventricle to expand and fill with enough blood. Heart failure can be right-sided or left-sided, but right-sided failure often results from left-sided failure. Although isolated right-sided failure can occur due to pulmonary hypertension resulting from pulmonary embolism, it is uncommon. Often, left-sided failure causes blood to back up in the lungs, thus increasing pressure in the pulmonary circulation and placing a burden on the right side of the heart, which leads to right-sided failure. Left-sided failure can result from an overloaded left ventricle (LV) (due to aortic stenosis or hypertension) or a weakened LV (due to post-myocardial infarction). Heart failure patients can exhibit decreased cardiac output (forward failure), increased atrial and venous pressure (backward failure), or both (Braunwald, 2001; Schoen, 1999).

The myocardium tries to compensate for the increased burden on the heart. One of the common ways it does this is with the development of ventricular hypertrophy (see Figure 1). Depending on the stimulus (pressure overload or volume overload), the ventricles will increase their mass in one of the two patterns shown in Figure 1. A

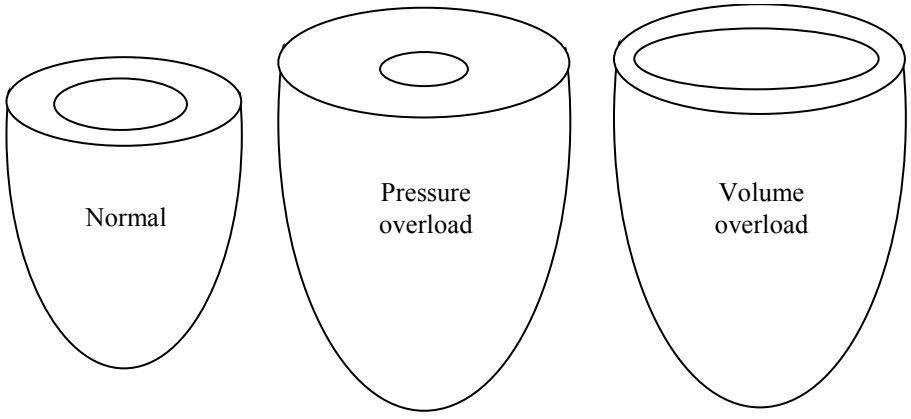

Figure 1: Patterns of hypertrophy. The figure on the left represents a normal ventricle. The central figure shows a concentric hypertrophic pattern, which results from pressure overloading. The far right figure represents eccentric hypertrophy as a result of volume overloading.

pressure-overloaded ventricle exhibits increased wall thickness and normal or reduced cavity diameter. This type of hypertrophy is called concentric hypertrophy. With this pattern of hypertrophy, the cross-sectional area of the myocytes increases. A volume-overloaded ventricle develops eccentric hypertrophy, in which muscle mass increases and the ventricle becomes dilated (i.e. ventricular diameter increases). In this case, myocytes elongate in the axial direction. Regardless of the type of hypertrophy, the heart may be able to compensate for the increased burden in this way for some time. Ultimately, the function of the myocardium can deteriorate into heart failure and the ratio of wall thickness to cavity diameter will decrease, placing more stress on the myocardium which causes further dilation (Braunwald, 2001; Omens, 1998; Schoen, 1999).

There are a number of factors that can cause the ventricle to begin the remodeling process that leads to hypertrophy. These events can be acute, as in myocardial infarction (MI) or an infection, or they can be chronic, as in hypertension or valvular disease. Whatever the cause, the myocardium initially responds by trying to compensate for the increased workload. For example, after MI, the early stages of remodeling involve the breakdown of the collagen matrix, which results in the loss of the high level of organization of the myocytes at the site of the infarct. The cells slip from their positions as the matrix breaks down, and the wall begins to thin. This increases stress on the entire ventricle, which induces hypertrophy of the myocytes (Paul 2003). Similarly, hypertension increases ventricular pressure (and thus wall stress), which affects gene expression, protein synthesis, ECM structure, and the capillary-to-myocyte ratio (Kenchaiah and Pfeffer, 2004). Collagen accumulates in the ECM as a result of increased production and decreased degradation. This can affect the movement of the myocytes and the compliance of the ventricle (Cleutjens et al., 1995). Eventually, these factors cause the ventricle to transition from compensation to failure.

Although many animal models have been used to study ventricular hypertrophy and congestive heart failure, they often involve surgical procedures and varying amounts of time for the condition to develop (Emery and Omens, 1997; Feldman et al., 1993;

Inoko et al., 1994; LeGrice et al., 1995b). However, the Dahl salt-sensitive rat develops systemic hypertension with the addition of sodium to its diet. Inoko et al. showed that when a high-salt diet is initiated at an appropriate age, these rats have a life span of 4-5 months and develop concentric LV hypertrophy. Subsequently, the rats consistently deteriorate from compensatory hypertrophy to heart failure without any other intervention. The heart failure that results is due to decreased contractile function of the myocardium and not cell damage or tissue loss. There is also a Dahl salt-resistant rat that can serve as a control for any experiments involving the salt-sensitive rats. The salt-resistant rats are genetically related to the salt-sensitive rats and do not exhibit hypertension when fed a high-salt diet (Inoko et al., 1994). Due to the benefits of the Dahl salt-sensitive rats as an animal model for CHF, they (and their salt-resistant relatives) will be used in the future to study and quantify the laminar architecture of healthy and diseased hearts using the imaging method developed in this thesis.

Objectives

The heart is constantly undergoing growth and remodeling. Growth of the heart refers to an increase in wall mass, while remodeling refers to a change in internal structure due to redistributed constituents. Growth and remodeling changes take place when the heart is in a healthy state as well as in a diseased state like CHF. Arguably, the first step in developing reasonable treatments and/or tissue-engineered replacements for the many Americans suffering from CHF is to understand how the myocardium responds to its mechanical environment. To do so, the cardiac microstructure needs to be characterized so the connection between cellular/matrix processes and cardiac function can be made. Because there is a large transmural variation in shear strain, it is possible that there is also a transmural variation in the laminar structure of the heart. This structure must be quantified in order to provide a physiological understanding of how the heart grows and remodels as it does in congestive heart failure. Many of the techniques that have been used to investigate the microstructure of the myocardium require staining the tissue with toxic chemicals in order to enhance the contrast between collagen and

myocytes. This thesis will focus on developing efficient imaging and image processing methods that will reveal the microstructure of the heart while minimizing the use of harmful chemicals.

BACKGROUND

The Structure of the Heart

The heart is a four-chambered muscular organ that lies in the center of the thoracic cavity. It is shaped somewhat like an inverted cone, with the base lying behind the sternum and the apex pointed down toward the left side of the body. It consists of two atria and two ventricles. Poorly oxygenated blood enters the right atrium (RA) from the venous circulation via the venae cavae. From here it flows into the right ventricle (RV), which pumps the blood to the pulmonary circulation where it is re-oxygenated. One-way valves prevent backflow of blood between the RV and RA (tricuspid valve) and the pulmonary artery and the RV (pulmonic valve). Freshly oxygenated blood moves from the pulmonary circulation into the left atrium (LA) via the pulmonary veins and then into the left ventricle (LV). The LV is responsible for pumping blood through the systemic circulation. The mitral valve prevents blood in the LV from flowing back into the LA, and the aortic valve prevents blood in the aorta from flowing back into the LV. The interventricular septum separates the RV and the LV.

Cardiac muscle tissue is called myocardium. It consists of two main constituents: collagen and myocytes. Collagen is the protein that makes up the majority of the extracellular matrix (ECM). In myocardium, the ECM consists primarily of types I and III collagen (Cleutjens et al., 1995; Humphrey, 2002). Bundles of collagen fibers extend circumferentially from each myocyte and connect to all adjacent myocytes (Caulfield and Borg, 1979). Myocytes are the cardiac muscle cells that are responsible for contraction. Cardiac muscle cells contract in a manner similar to that of skeletal muscle cells. Both cell types consist of sarcomeres containing thick filaments (myosin) and thin filaments (actin). Sarcomeres are arranged end-to-end and are the contractile units of muscle tissue (Humphrey, 2002). Shortening of a cell occurs when actin filaments slide along neighboring myosin filaments. Cardiac muscle differs from skeletal muscle in that the muscle cells branch and join adjacent cells to form a complex structure that works as a single unit (Berne and Levy, 2001; Caulfield and Borg, 1979).

The myocardium has a highly organized microstructure, and in this thesis the focus will be on the LV and the microstructure of the interventricular septum. The coordinate system that will be used to describe the left ventricle is illustrated in Figure 2. The three orthogonal directions are $\underline{e}_1$, the local circumferential direction, $\underline{e}_2$, the longitudinal or apex to base direction, and $\underline{e}_3$, the radial direction. The positive longitudinal direction runs from apex to base. The positive radial direction for the LV points outward from the chamber. Using the right hand rule with the thumb pointing in the direction of the positive longitudinal direction, the positive circumferential direction can be determined. The interventricular septum is considered to be a part of the LV, so the positive circumferential direction always goes from the posterior side of the septum to the anterior side (see Figure 3). A continuum of muscle fibers makes up the ventricles, and the fiber angle, α, is measured with respect to the positive circumferential direction. The angle of these muscle fibers changes with wall depth. Streeter showed that on the epicardial surface of a contracted canine LV, α is near -90º, at the midwall it is 0º, and on the endocardial surface, it is near +90º (Streeter, 1979). Figure 4 shows a schematic representation of this variation in fiber angle. Note that the figure is meant to illustrate the change in fiber angle with wall depth and not the distance between the fibers or the number of fibers.

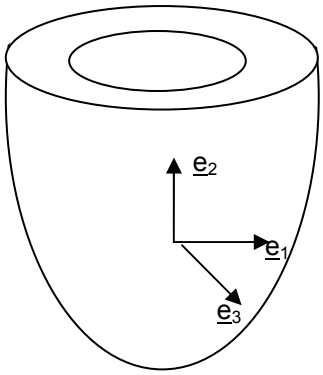

Figure 2: Coordinate system for the LV. The local circumferential direction is $\underline{e}_1$, the apex to base, or longitudinal direction is $\underline{e}_2$, and the radial direction (pointing outward from the LV cavity) is $\underline{e}_3$.

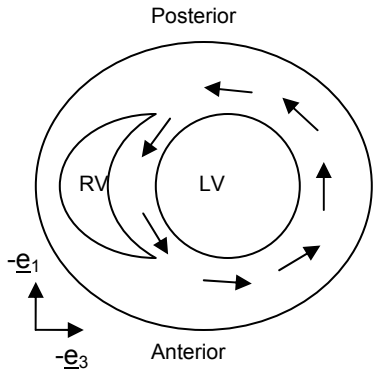

Figure 3: The right-hand rule. The thumb points from apex to base ($+\underline{e}_2$) in order to determine the positive circumferential direction ($+\underline{e}_1$). In the septum, the positive circumferential direction always goes from posterior to anterior.

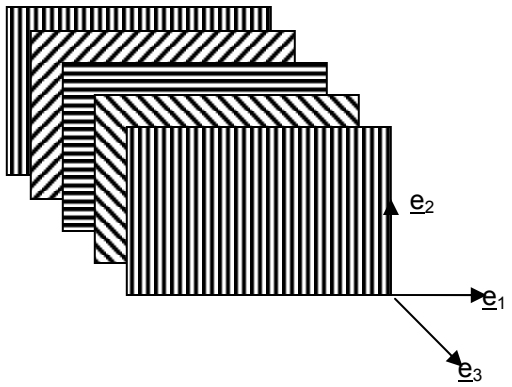

Figure 4: Transmural variation in fiber angle. The front surface represents the epicardium of the LV and the back surface represents the endocardium. The fiber angle runs from -90º on the epicardium to +90º on the endocardium.

The fundamental structural unit of the heart is the myolamina, a sheet of myocytes about four cells thick, which is surrounded by a collagen weave (LeGrice et al., 1995a). These sheets of cells branch and connect to adjacent sheets and appear to be "stacked" from apex to base (Costa et al., 1999). Gaps, or cleavage planes, are present between the myolaminae. It appears that these gaps allow large shearing deformation within the myocardium without the large stresses that would otherwise be expected. The sheet angle, β, is the angle that the myolaminae make with the radial direction when looking directly down the fiber direction. In addition to the cardiac coordinates described previously, a system of orthogonal fiber-sheet coordinates can also be defined. These coordinates can be obtained by two rotations of the cardiac coordinates. First, the coordinate system is rotated about the radial axis ($\underline{e}_3$) through the fiber angle α until the local circumferential axis ($\underline{e}_1$) lines up with the local fiber direction and becomes the fiber axis $\underline{e}_f$. The coordinates are then rotated about $\underline{e}_f$ through the sheet angle β giving the sheet axis $\underline{e}_s$. The sheet plane is formed by these two orthogonal axes. The sheet normal axis $\underline{e}_n$ is orthogonal to this sheet plane (Costa et al., 1997). The positive direction of the normal axis is determined by taking the cross product of the fiber axis and the sheet axis. Figure 5 shows the rotations that transform the cardiac coordinates into fiber-sheet coordinates.

In healthy hearts of swine, the organization of the myolaminae varies transmurally[1]. In the sub-epicardium of these swine hearts, there are very few myolaminae. In the midwall, there are many layers that are highly organized and uniformly oriented. In the sub-endocardium, there are many intersecting myolaminae. Similar variations in structure are visible in rats[2] and dogs, but this laminar structure has not been studied in humans (LeGrice et al., 1995a). Costa et al. showed that much more shear deformation occurs at the inner wall of the healthy canine LV than at the outer wall (Costa et al., 1999). From these data, it seems that the large number of myolaminae

[1] Unpublished observations by John Criscione, Assistant Professor, Department of Biomedical Engineering, Texas A&M University.
[2] Unpublished observations by John Criscione and Kristen Hudson (author of this thesis).

corresponds to the greatest amount of deformation. To better understand this idea, the laminar organization of the myocardium must be quantified in both healthy and diseased hearts.

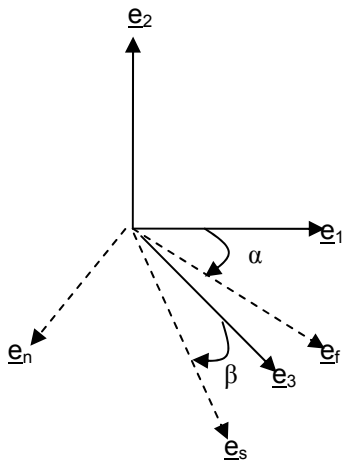

Figure 5: Cardiac and fiber-sheet coordinates. Solid lines represent the cardiac coordinate system ($\underline{e}_1$, $\underline{e}_2$, $\underline{e}_3$) while the dashed lines represent the fiber-sheet coordinate system ($\underline{e}_f$, $\underline{e}_s$, $\underline{e}_n$). First, the cardiac coordinates are rotated about $\underline{e}_3$ such that $\underline{e}_1$ rotates through α. Next, the orthogonal components are rotated about $\underline{e}_f$ such that $\underline{e}_3$ rotates through β.

Previous Work

One of the objectives of imaging myocardium has been to study changes in the structure of the heart in various pathologic conditions (Emery and Omens, 1997; Yang et al., 2002). More recently, investigators have been interested specifically in quantifying the laminar organization of the heart to better understand how it grows and remodels (Costa et al., 1997, 1999; LeGrice et al., 1995a). Many different methods have been used to image myocardium in the past. Caulfield and Borg used scanning electron microscopy to investigate the collagen network of the heart (Caulfield and Borg, 1979). Another group has used silver impregnation of myocardium to view collagen with light microscopy and electron microscopy (Robinson et al., 1983). Yet another group used confocal laser microscopy to view myocardium (Young et al., 1998). Several groups have stained myocardium with picrosirius red (PSR), which enhances the birefringence of collagen when used with polarized light (Junqueira et al., 1979; Weber et al., 1994). Linearly and circularly polarized light have both been employed to view the collagen structures (Emery and Omens, 1997; Junqueira et al., 1979; Weber et al., 1994; Whittaker et al., 1989, 1994). Only recently has polarized light been used to image unstained myocardium. Tower and Tranquillo used unstained porcine heart valve leaflets to demonstrate their method for generating fiber alignment maps of tissue because of the spatially varying alignment of fibers within the leaflets (Tower and Tranquillo, 2001).

Several groups have used polarization microscopy to image skin for the purpose of investigating both the surface and subsurface structures (Anderson, 1991; Demos and Alfano, 1997; Jacques et al., 2000, 2002). In these studies, detailed images of the surface of the skin were obtained when the input polarizer and the analyzer were aligned with their polarization axes parallel to one another (denoted I_{par} by Jacques et al., 2000). This configuration essentially enhanced the surface glare, thus showing the texture and elevation of the skin. Photons that were backscattered from the surface had little opportunity to depolarize and as a result were still polarized parallel to the incident light. When the input polarizer and analyzer were aligned with their axes perpendicular to one

another, the image contained information from beneath the surface (denoted I_{per} by Jacques et al., 2000). In this configuration, surface detail and glare were eliminated because the photons penetrated deeper into the tissue and were depolarized. Jacques et al. combined the parallel and perpendicular images to obtain a third image that they called the "polarization image" denoted by I_{pol} in Equation 1.

$$I_{pol} = \frac{I_{par} - I_{per}}{I_{par} + I_{per}} \quad (1)$$

By subtracting the perpendicular image from the parallel image in the numerator of Equation 1, randomly polarized light is eliminated from the polarization image. The denominator, which is both images added together, represents a normal white light image. By taking the ratio of these two algebraic combinations, the investigators were able to eliminate the effects of variations in illumination and variations in melanin content on the image (Jacques et al., 2000, 2002).

Theory

Collagen is birefringent, meaning it is anisotropic with respect to the index of refraction and can cause double refraction (Pedrotti and Pedrotti, 1993). When polarized light passes through a birefringent material, it is resolved into two rays that are cross-polarized and traveling at different velocities due to the anisotropic structure of the material. One of these rays travels along the fast transmission axis while the other travels along the slow transmission axis (Whittaker et al., 1989). Materials can possess form birefringence or intrinsic birefringence. Form birefringence results from an alignment of non-spherical molecules or a highly elongated shape. Intrinsic birefringence results from the lack of a symmetry axis present in optically active protein molecules (Arimoto and Murray, 1996; Pantic-Tanner and Eden, 1999). Myocardium possesses both types of birefringence as a result of its content and structure, but form birefringence contributes much more to polarization microscopy images of unstained tissue (Arimoto and Murray, 1996; Oldenbourg et al., 1998). The ordered arrangement of fibers in myocardium makes it well-suited for polarization microscopy. Additionally,

collagen is more birefringent than cardiac myocytes, meaning that the appearance of the collagen weave surrounding the myolaminae should be enhanced with this technique (Jouk et al., 1995; Wolman, 1975).

METHODS

Sample Preparation

First and foremost, approval from the animal care and use committee at Texas A&M University (AUP # 2002-41) was obtained for this investigation. A healthy Sprague-Dawley adult rat was sacrificed in a carbon dioxide chamber and the heart was excised. After the rat heart was fixed in 10% phosphate buffered formalin at a pressure of 1 kPa for one week, the interventricular septum was dissected out. The septum is ideal for imaging because it has uniform thickness with minimal curvature and is fairly smooth. There are no trabeculae or papillary muscles on the LV side. On the RV side, there are very few trabeculae and small papillary muscles. Once the septum was removed, cuts were made parallel to the circumferential-longitudinal plane (i.e. in the direction of $\underline{e}_2$) to create four slices of approximately equal thickness. The septum was 2.92 mm thick and the slices were approximately 0.73 mm thick. As each cut was made, the freshly cut face was viewed with an Olympus SZX12 Research Stereomicroscope (Olympus Optical Company, Ltd., Tokyo, Japan). The sample was positioned so that the $\underline{e}_2$ direction was parallel with the x-axis of the camera and an initial image showing the whole slice was taken. Then, approximately one third of the tissue was imaged at the basal end of the slice. The basal one-third of every slice was selected because the insertion of a papillary muscle creates fiber disarray in the two-thirds of the slice near the apex. These images were taken for all faces except face 5 (the RV surface) because papillary muscle on the RV wall makes it difficult to determine one fiber direction on that face. Paper was glued to some of the faces to indicate the orientation. Figure 6 is a diagram of a top-down view of the slices made from the interventricular septum. The thick dashed lines represent the paper backing that was glued to the slices. On each slice, a suture was glued to the posterior-apex corner to maintain orientation. The slices of the septum were infiltrated with JB-4 tissue embedding resin (Polysciences, Inc., Warrington, PA). JB-4 media was used because, unlike paraffin embedding, it does not require dehydration of the tissue by graded alcohols. Dehydration grossly distorts the

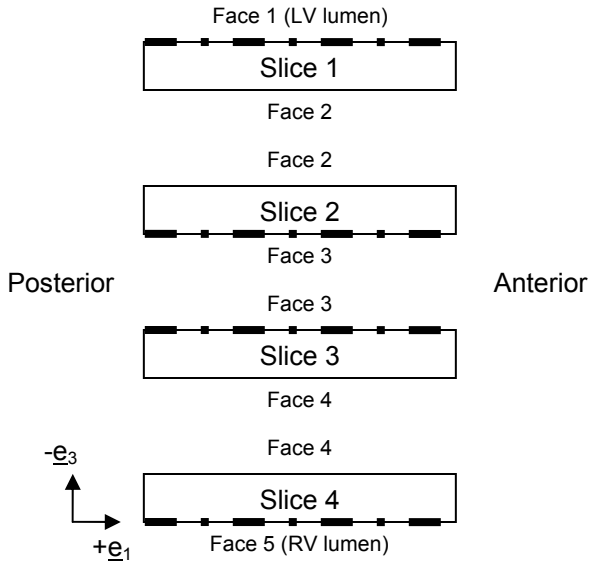

Figure 6: Top-down view of slices made from the septum. Slices are numbered from the LV lumen (Slice 1) to the RV lumen (Slice 4). Heavy dashed lines indicate where paper backing was glued to the samples.

tissue, which compromises measurements of any microstructural elements. Although acceptable for qualitative histology, such distortion introduces a systematic error in quantitative histology measurements. Systematic error cannot be eliminated with averaging. After infiltrating in the JB-4 for one week, the slices needed to be cut cross-fiber in order to view the laminar structure.

Sample Orientation and Imaging

As mentioned before, the fiber angle, α, is measured with respect to the positive circumferential direction (+$\underline{e}_1$). Equation 2 gives the positive fiber direction in terms of the circumferential and apex-base directions. The cross-fiber direction is perpendicular to the fiber direction, and Equation 3 can be used to determine which way is positive.

$$+\,fiber = \cos(\alpha)\underline{e}_1 + \sin(\alpha)\underline{e}_2 \tag{2}$$

$$+\,crossfiber = -\sin(\alpha)\underline{e}_1 + \cos(\alpha)\underline{e}_2 \tag{3}$$

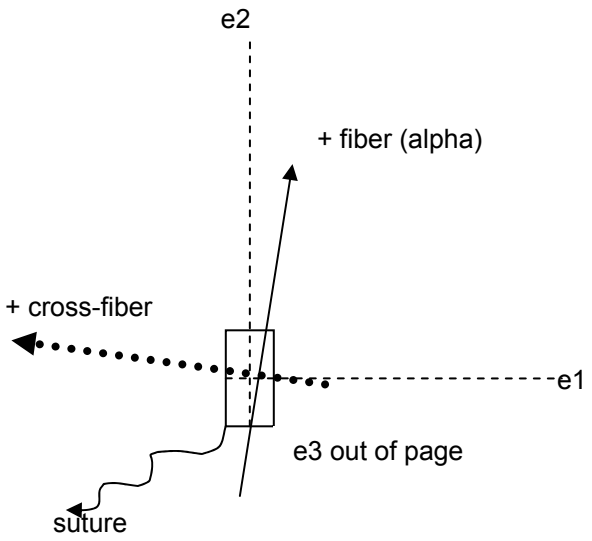

Figure 7: Sample cutting template. The solid arrow represents the average fiber direction for a slice. The heavy dotted arrow is the cross-fiber direction and is where the cut should be made.

The angle on each face (except face 5) was measured from the images taken with the Olympus SZX12 Research Stereomicroscope using ImageJ (NIH, Bethesda, MD). On each image, the angle was measured, providing the fiber angle for each face. For slices 1 through 3, the average of the fiber angles from the two faces was used as the overall fiber angle. Due to fiber disarray, the fiber angle on face 5 could not be measured so linear regression was used to extrapolate the fiber angle to the RV surface.

In order to view the myolaminae, the samples had to be viewed looking directly down the fiber. To do this, a cut in each slice had to be made perpendicular to the slice's overall fiber angle. Equation 3 was used to determine which way the positive cross-fiber direction pointed. In order to simplify the process of making cuts at specific angles, templates for each slice were created that indicated $+\underline{e}_1$ and $+\underline{e}_2$ as well as the positive fiber direction and the positive cross-fiber direction. Each slice was glued to the appropriate template with its paper backing face down. A cut was made along the +cross-fiber line in the basal one-third of each slice. Figure 7 shows a sample cutting template. The dotted arrow indicates where the cut should be made and points in the

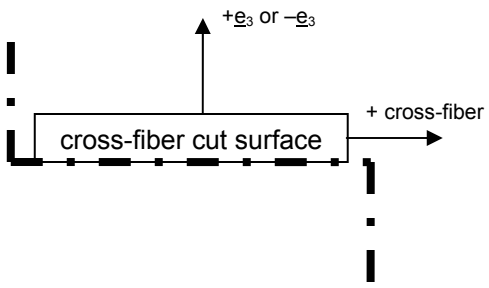

Figure 8: Diagram of cross-fiber surface of slice (i.e. looking directly down the fiber). Again, heavy dashed line represents paper glued to the sample. The paper is folded away from the sample on the side that is the positive cross-fiber direction.

positive direction. After the cross-fiber cuts were made, the paper was folded so as to indicate which side was the positive cross-fiber direction. As shown in Figure 8, the paper (indicated by the heavy dashed line) on the side of the positive cross-fiber direction was folded away from the sample. The slices were placed in tissue molds with the cross-fiber cut face down. Additional JB-4 and hardener was used to fill the molds and then a plastic block was placed in the mold. The sample was allowed to harden overnight.

Histological sections approximately 10 μm thick were made from the cross-fiber surface of slice 1 of the sample. These sections were viewed at 100x magnification on an Olympus CX31 Biological Microscope (Olympus America Inc., Melville, NY), which was modified to hold two Leica rotatable polarizers. A specially adapted mounting device was used to mount a Kodak EasyShare DX4900 Digital Camera (Eastman Kodak Company, Rochester, NY) to a wide-angle ocular. The polarizer and analyzer were rotated so as to capture all possible input and output combinations, 16 in all. The analyzer was limited to 45º rotation increments: horizontal (H), minus 45º (M), vertical (V), and plus 45º (P). For each combination, an image was taken at 100x magnification. From the raw images, a region of interest (ROI) was selected that measured 800 pixels by 800 pixels and had its upper left corner at the pixel coordinates (1300, 632). This ROI is represented by the box in Figure 9.

All polarization combinations (16 in all) are given by two letters, the first corresponding to the input polarizer and the second corresponding to the analyzer. The possible polarization states are horizontal (H), minus 45º (M), vertical (V), and plus 45º (P). All matrices that were found in this research correspond to the matrix below.

$$\text{Matrix} = \begin{matrix} \text{HH} & \text{HP} & \text{HV} & \text{HM} \\ \text{PH} & \text{PP} & \text{PV} & \text{PM} \\ \text{VH} & \text{VP} & \text{VV} & \text{VM} \\ \text{MH} & \text{MP} & \text{MV} & \text{MM} \end{matrix}$$

Image Processing Techniques and Angle Determination

Due to the quality of the equipment, a non-uniform intensity variation was visible in the images and needed to be reduced through image processing. In the raw images, there is approximate mirror symmetry in the intensity about the line created by two bright areas. These bright areas are represented by the circles in Figure 9. To obtain the background intensity image for the ROI, the mirror point of the background (i.e. where there is no tissue) was found for each corresponding point in the ROI. The intensity value for each background pixel was used as the background intensity for each mirrored pixel in the ROI. This yielded a background intensity image for the entire ROI that represented what the image would look like without any tissue present. The background intensity was fit to a smooth bicubic function, which gave the intensity as a function of position. Figure 10 shows the raw VP background image and the smoothed VP background image. Notice that the many spots visible in the raw image are eliminated in the smoothed image. Figure 11 is a plot of the intensity at each pixel location for the raw and smoothed background images. Sudden changes in intensity are eliminated in the smoothed plot. The intensity of the ROI was normalized by dividing by the local background intensity and multiplying by the intensity of the center point of the ROI, which will be referred to as node 4 (pixel location 400, 400). This algorithm is given by Equation 4.

$$Matrix_{adjusted\_ROI} = \frac{Matrix_{raw\_ROI}}{BG_{fit}} \times I_{BG\_(400,400)} \tag{4}$$

$Matrix_{raw\_ROI}$ refers to the matrix of raw ROI images, BG_{fit} refers to the smoothed background intensity, and $I_{BG\_(400,400)}$ refers to the background intensity of node 4 in the matrix element of interest. This resulted in a matrix of adjusted images of the ROI which had a more uniform intensity. Figure 12(a) shows the raw ROI image (VP) and 12(b) shows the adjusted ROI image. The white arrow is pointing to a brighter region that is eliminated in the adjusted image.

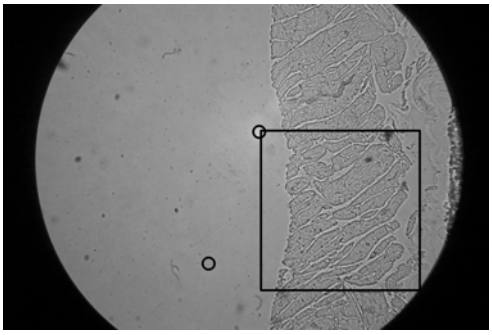

Figure 9: Raw VP image showing ROI and bright spots. The square is the 800x800 region of interest. The two circles represent the bright spots that make up the line about which there is mirror symmetry in intensity.

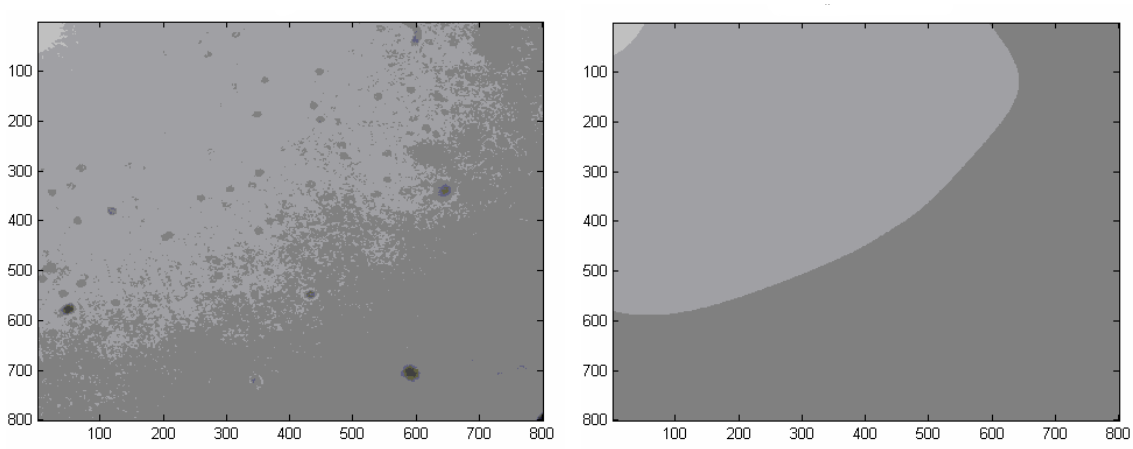

(a) (b)

Figure 10: Background images for VP. The raw image (a) has a speckled appearance that is eliminated in the smoothed image (b).

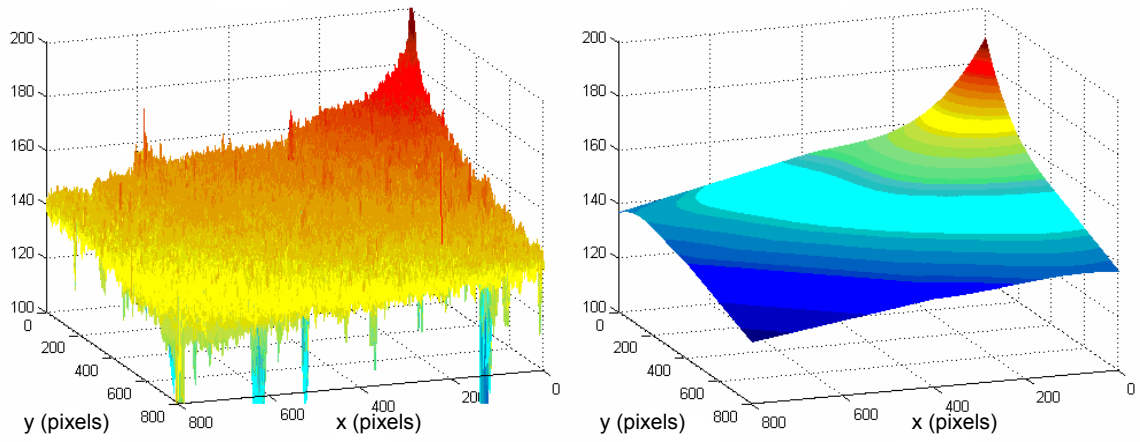

(a) (b)

Figure 11: Background intensity plots for VP. Intensity (vertical axis) is plotted with position on the raw background image (a) and after the background intensity was fit to a smooth bicubic function (b).

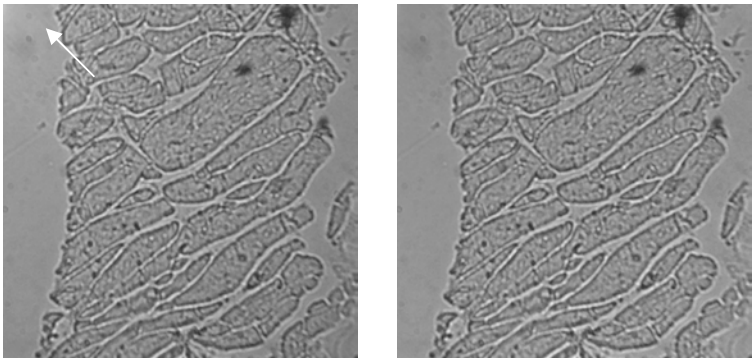

(a) (b)

Figure 12: Progression from raw ROI image to adjusted ROI image. The image on the left is the raw VP ROI. The image on the right resulted from dividing the raw ROI by the background image and multiplying by the intensity of the center point. Note that the bright region in the upper left corner is eliminated.

In addition to the non-uniform intensity, the camera gain needed to be accounted for because it was variable. Equation 5 demonstrates the relationship between the angle made between the axis of transmission for the polarizer and the analyzer and the intensity of transmitted light (Pedrotti and Pedrotti, 1993). When the polarizers are aligned, the maximum amount of light is transmitted; when they are crossed, the minimum amount is transmitted.

$$I_{BG\_(400,400)} = cgain \times I_{BGHH\_(400,400)} \times \cos^2(\theta) \quad (5)$$

$I_{BG\_(400,400)}$ refers to the background intensity of node 4 in the image of interest, while $I_{BGHH\_(400,400)}$ refers to the background intensity of node 4 in the HH image. θ is 0º when the polarizers are parallel and 45º when they are offset by 45º. The camera gain (denoted cgain) was assumed to be 1.0 for the HH configuration because the maximum amount of light is transmitted when the polarizers are aligned. Equation 5 was rearranged and used to calculate the camera gains when the polarizers were aligned or offset by 45º (Equation 6).

$$cgain = \frac{I_{BG\_(400,400)}}{I_{BGHH\_(400,400)} \cos^2(\theta)} \tag{6}$$

When the polarizers were crossed (i.e. θ=90º), the camera gain was found by comparing the intensity of the black region outside the field of view (i.e. extra-ocular region) in each image (denoted $I_{min\_\perp}$) to the non-crossed image with the brightest extra-ocular region (denoted I_{min_VP}) using a ratio of camera gain to minimum intensity outside the field of view (Equation 7).

$$\frac{cgain_{\perp}}{I_{min\_\perp}} = \frac{cgain_{VP}}{I_{min\_VP}} \tag{7}$$

In this data set, VP had the brightest extra-ocular region of all the non-crossed images because the camera gain was the highest. The camera gain was adjusted automatically and could not be controlled on the camera that was used. The elements of the matrix of adjusted ROI images were divided by the corresponding camera gains, resulting in a matrix of images in which the background and camera gain had been accounted for (Equation 8).

$$Matrix_{NoBG\_NoGain} = \frac{Matrix_{adjusted\_ROI}}{cgain} \tag{8}$$

These images accounted for the differential gain of the camera and represented the images that would have been obtained if the camera gain could have been set. A matrix of scalars (called $Matrix_{I\_BG}$) was obtained by dividing the intensity at node 4 of each element of the matrix of background images by the corresponding camera gain. These numbers represented the value of the intensity of the background (which was made more uniform) for each element in the matrix of images in which the background and camera gain had been accounted for. These background intensities were subtracted from the images adjusted for background and camera gain to obtain a difference matrix (called $Matrix_{difference}$). This formula is shown in Equation 9.

$$Matrix_{difference} = Matrix_{NoBG\_NoGain} - Matrix_{I\_BG} \tag{9}$$

To enhance the contrast between the collagen and myocytes, the elements of this difference matrix were squared and then summed, and then the square root was taken, giving the magnitude of the difference matrix (Equation 10).

$$Magnitude_{difference} = \sqrt{\sum_i (Matrix_{NoBG\_NoGain_i} - Matrix_{I\_BG_i})^2} \quad (10)$$

This magnitude was a scalar image that represented how the sample differed from the background at each pixel. This scalar image was scaled so the maximum pixel value was 256, which is the brightest intensity value for pixels in a gray-scale image (Equation 11)

$$Magnitude_{scaled} = \frac{Magnitude_{difference}}{Max_{difference}} \times 256 \quad (11)$$

$Max_{difference}$ refers to the maximum intensity value in the image of the magnitude of the difference matrix.

Data points were obtained by outlining each myolamina in an image using the mark and count tool in ImageJ (NIH, Bethesda, MD). These pixel values were fed into a program that calculated vectors representing the major and minor axes of each sheet. The sheet angle, β, for each sheet was found from the unit vector representing the major axis of that sheet. A histogram of the data was plotted for slice 1 and an overall value for β was estimated from this plot (for more details see Jetton, 2004). To compare the raw and processed images, the angle for one specific sheet was found from a raw image and the magnitude of the difference matrix image, and these values were compared.

To determine if the contrast between the collagen and myocytes was enhanced, a small region that included the edge of a myolamina was selected. This region was a square 60 pixels on each side and is shown as a box in Figure 13. The whole ROI was not used because there were dark spots present in all of the images that were not a part of the sample. The arrow in Figure 13 points to one of these spots. Within the square region, the maximum intensity value was compared to the minimum intensity value. If the intensity range of the magnitude of the difference matrix is greater than that of any of the raw images, the contrast is greater.

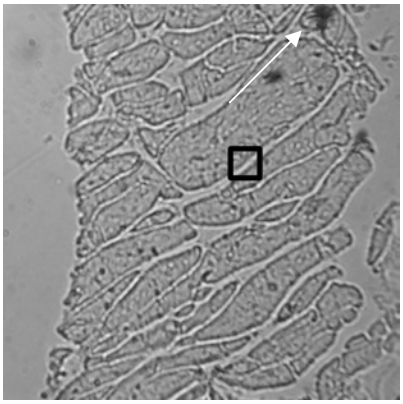

Figure 13: Region in which contrast enhancement was analyzed. The box is 60 pixels on each side, and the ratio of maximum intensity to minimum intensity in this region was compared for all the raw images and the image of the magnitude of the difference matrix.

RESULTS

In this section, raw images and the results obtained from the image processing techniques on sections from slice 1 are reported. The cross-fiber cut surfaces were imaged with all 16 polarization combinations. Figure 14 includes all 16 raw images. From the raw images, a region of interest (ROI) was selected from approximately the center of the sample. The ROI was a square, 800 pixels on each side, and was illustrated previously by the box in Figure 9. Figure 15 shows the ROIs for slice 1. In the raw images, there is approximate mirror symmetry in the intensity about the line created by the bright spot near the center and a lower bright spot that is more difficult to see. These spots were represented by the circles in Figure 9. The background intensity images represent the images that should be obtained without any tissue present. They were obtained by mirroring the background area onto the area where the sample is located, pixel by pixel, and then smoothing the images. These background images can be seen in Figure 16. The intensity of the ROI was then normalized by dividing each image by the corresponding local background intensity and multiplying by the intensity of the center point of the corresponding ROI. This resulted in adjusted images of the ROI which had a more uniform intensity as shown in Figure 17.

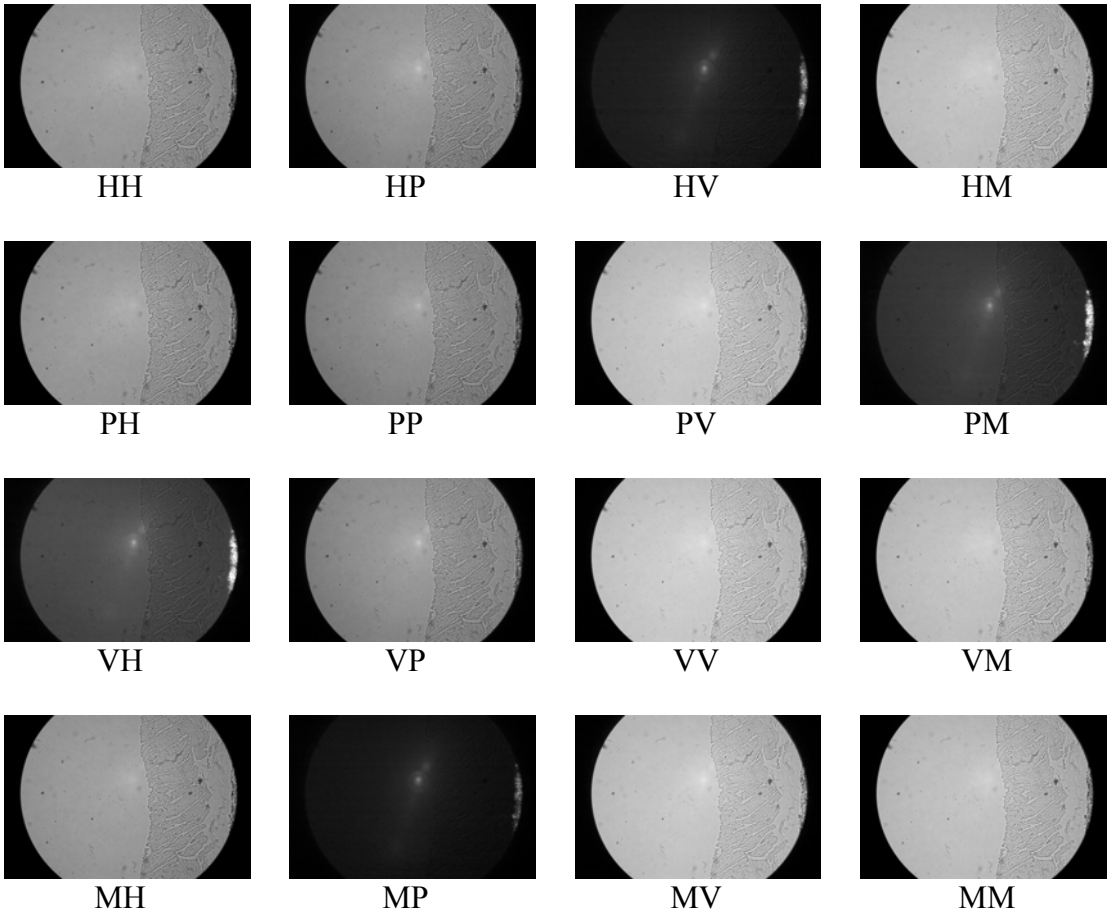

Figure 14: Raw polarization images. The positive cross-fiber direction is aligned with the y-axis of the image pointing up. Note that the myolaminae appear to be oriented at about 35º.

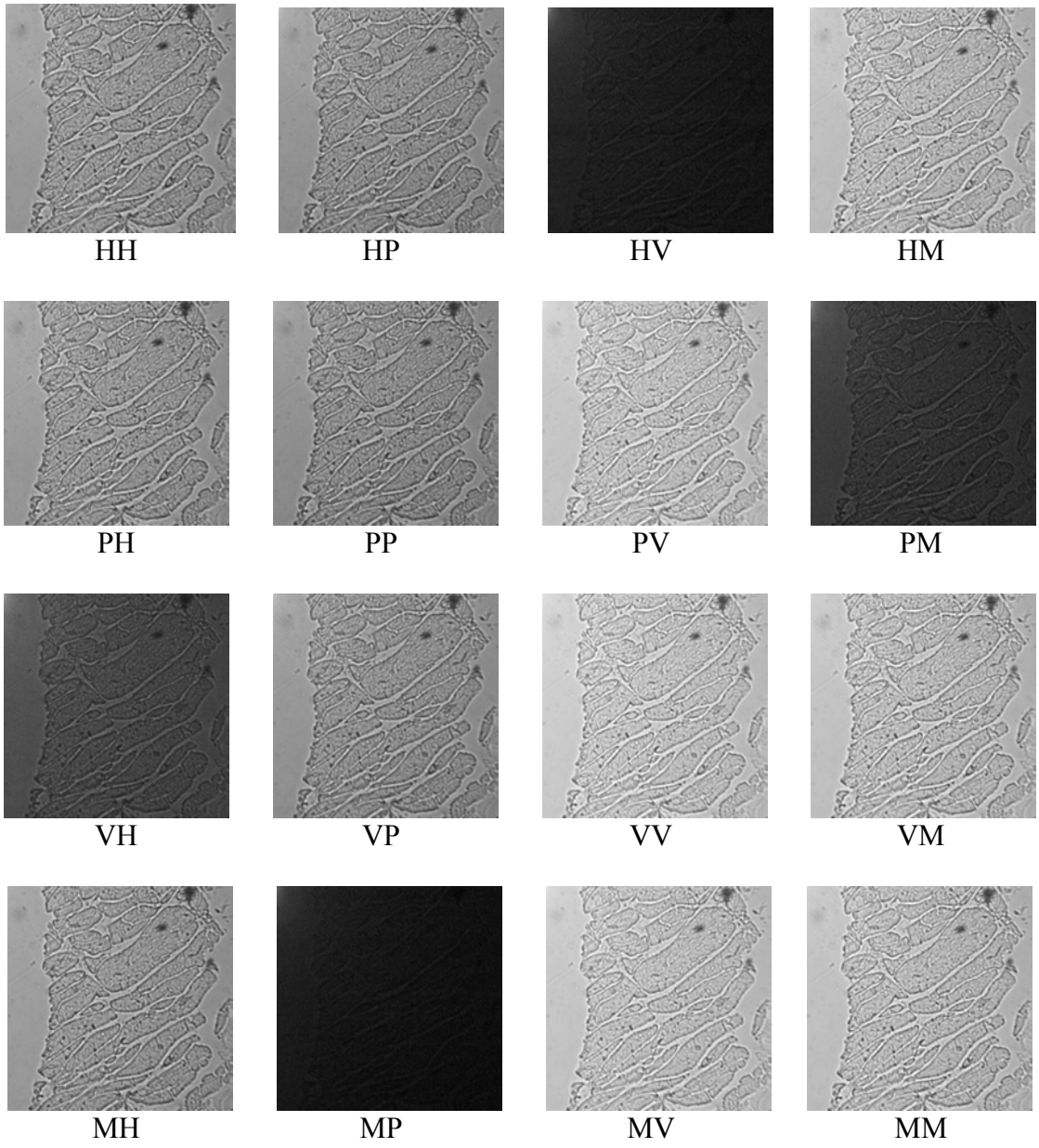

Figure 15: Regions of interest. These 800x800 regions are taken from the raw images. Note the intensity variation, specifically the bright area in the upper left corner of each of these images.

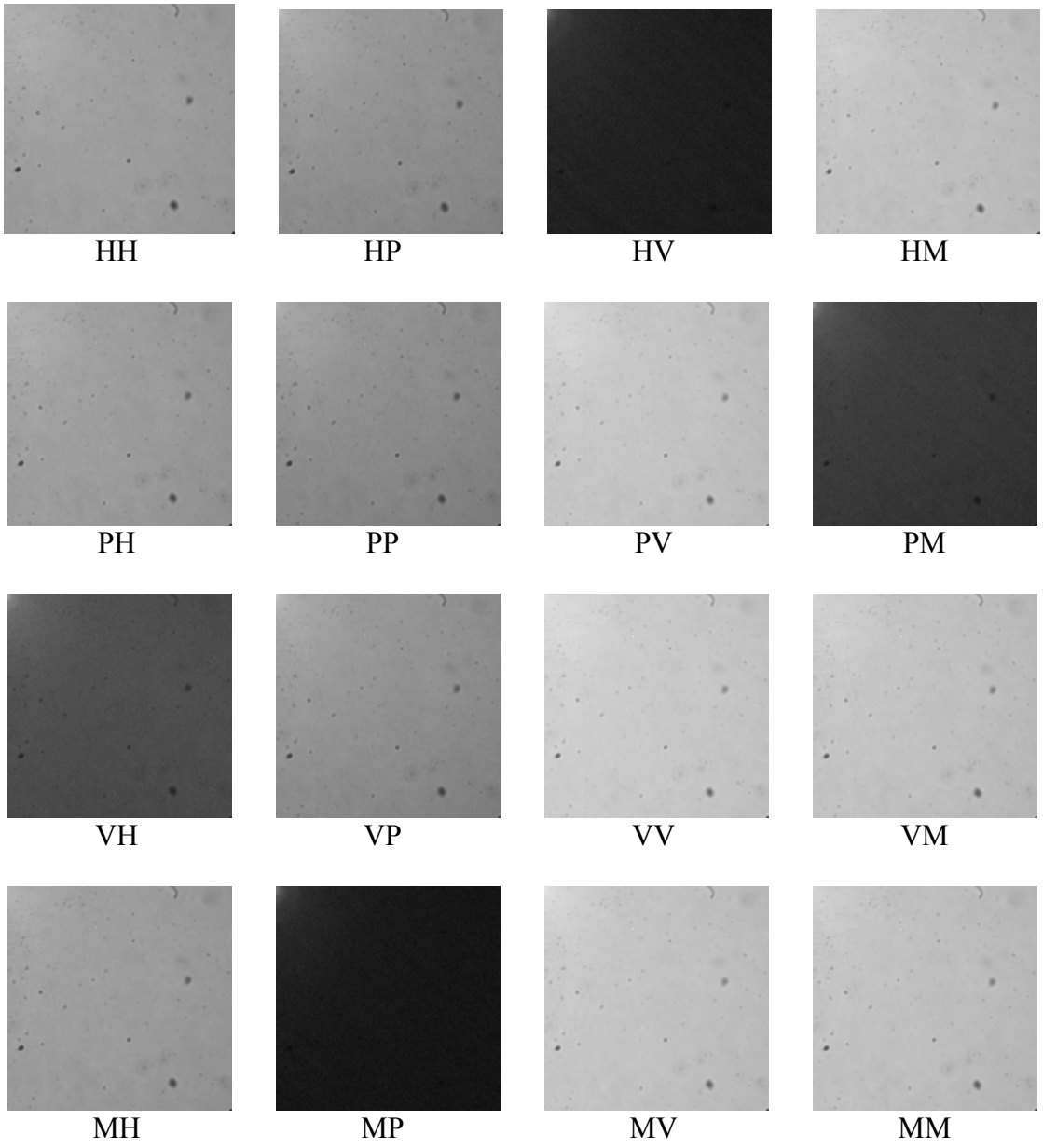

Figure 16: Background intensity images for ROI. These images show the intensity variation that should appear without any tissue present.

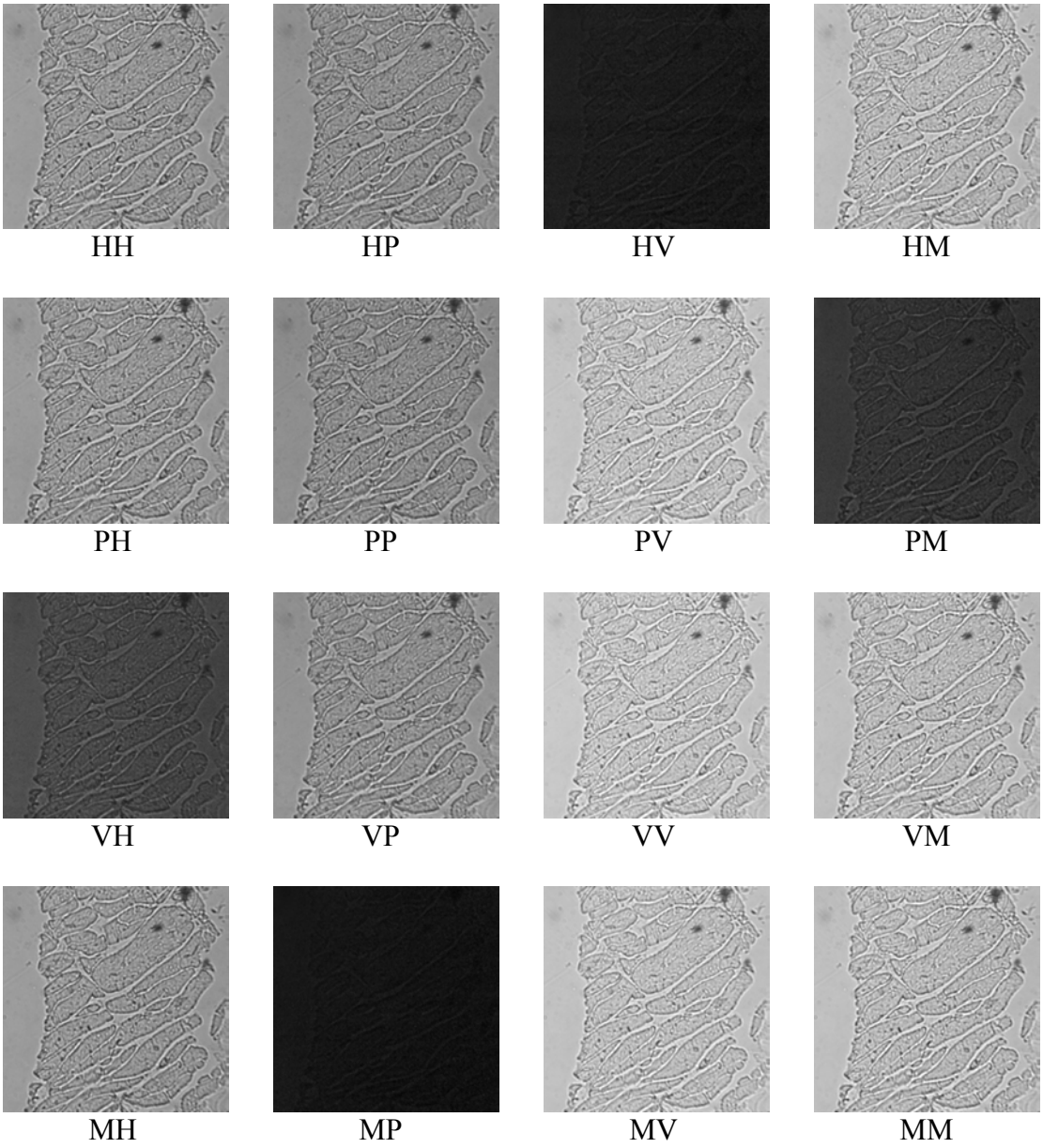

Figure 17: Adjusted images for ROI. The intensity variation for these images was lessened using image processing techniques. Note the absence of the bright spot that was in the upper left corner of the raw ROI images.

The camera gains for each polarization combination were found to be

1.0000	1.8445	4.5117	2.4268
1.9851	0.8907	2.4936	4.2821
4.8955	1.8440	1.2775	2.4503
1.9823	3.6315	2.4617	1.2135

Each adjusted ROI image was divided by the corresponding camera gain, giving a matrix of images which is shown in Figure 18. The matrix of intensity values of the background at node 4 of each image ($Matrix_{I\_BG)}$ is

157.8491	78.9246	7.1880	78.9246
78.9246	157.8491	78.9246	13.4594
15.8398	78.9246	157.8491	78.9246
78.9246	6.6364	78.9246	157.8491

These background intensities were subtracted from the images adjusted for background and camera gain to obtain a difference matrix. The magnitude of the difference matrix is a scalar whose image is shown in Figure 19.

For slice 1, the overall fiber angle was estimated by taking the average of the fiber angles of each face on that slice (faces 1 and 2). This estimate for α was **72.325º**. The slice was cut perpendicular to the fiber direction so that the myolaminae could be viewed directly. The sheet angle, β, was determined for all of the sheets in the ROI of slice 1 using a raw ROI image (HH). Figure 20 is the histogram of the sheet angle data for slice 1. From these data, the estimate for the sheet angle β was **-23.605º** (for details see Jetton, 2004).

β for a specific sheet in slice 1 was measured in a raw ROI image (HH) and the final processed image. Figure 21 shows the raw image with the sheet outlined by data points. Note that the data points were not the actual ones used but are merely representative of a data set. For the raw image, the sheet angle for the sheet of interest was found to be **-39.726º**. For the processed image it was **-39.420º**, giving a percent difference of 0.77%. Note that these values were only measured for one specific sheet, and although different from the average angle of -23.605, they do fall within the histogram range found by Jetton (Jetton, 2004).

To determine if the contrast between the collagen and myocytes was enhanced in the image of the magnitude of the difference matrix, the ratio of maximum intensity to minimum intensity in a small region was used. A higher ratio indicates greater contrast. The matrix below shows the values for this ratio from the raw ROI images.

3.12	3.35	4.09	2.58
3.22	2.97	2.15	4.27
4.00	2.96	2.28	2.45
3.22	7.60	2.19	2.40

The raw image with the maximum contrast was MP (7.60). When this same ratio was calculated for the magnitude of the difference matrix image, it was found to be 22.67, indicating that the contrast was enhanced by almost threefold.

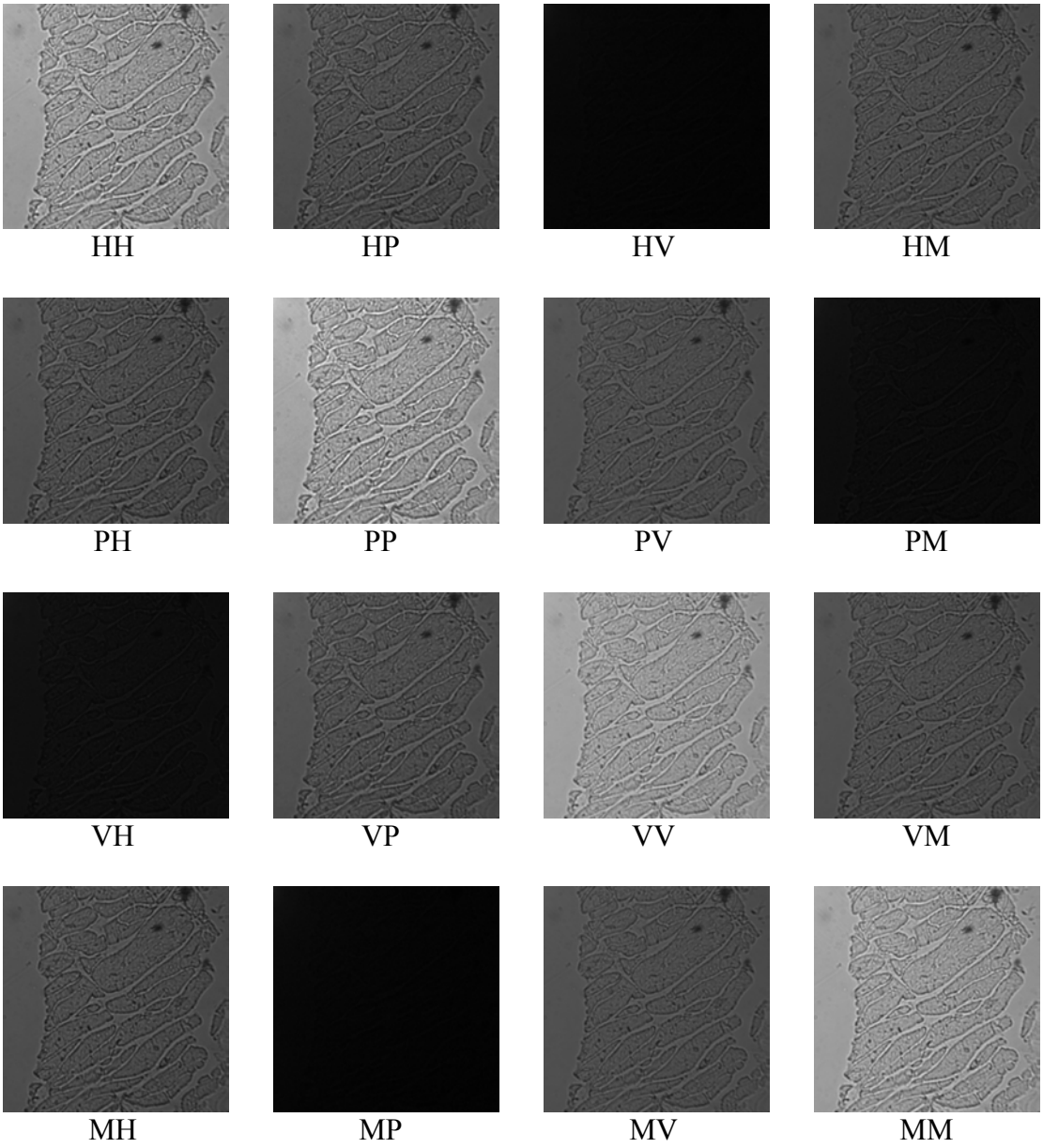

Figure 18: Images adjusted to account for variable camera gain. Adjusted ROI matrix elements were divided by the corresponding camera gains, the result being that all elements essentially have the same gain as the HH image.

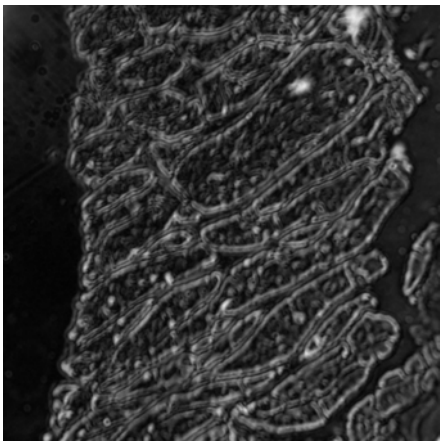

Figure 19: Image of the magnitude of the difference matrix. This image represents how the adjusted ROI differs from the background. Blurriness is most likely due to mis-registration of each of the 16 images. Because this processed image is the result of an algebraic combination of matrix elements, slight differences in camera position result in blurriness.

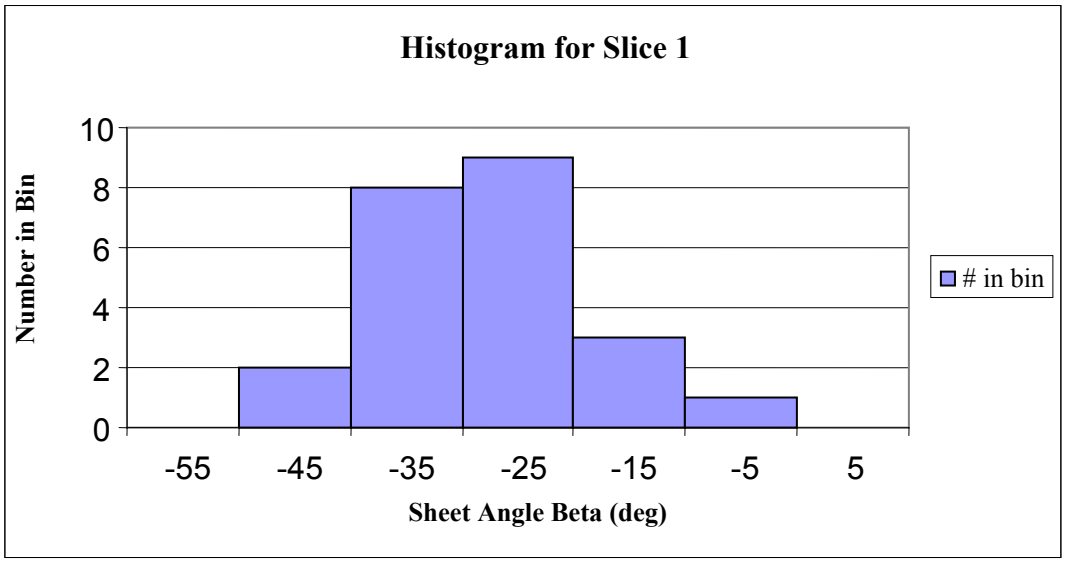

Figure 20: Histogram of sheet angle data for slice 1. Each bin is 10º wide and the number of sheets that falls within each bin is shown on the y-axis. The β estimate was determined from the average of the bin containing the most sheets.

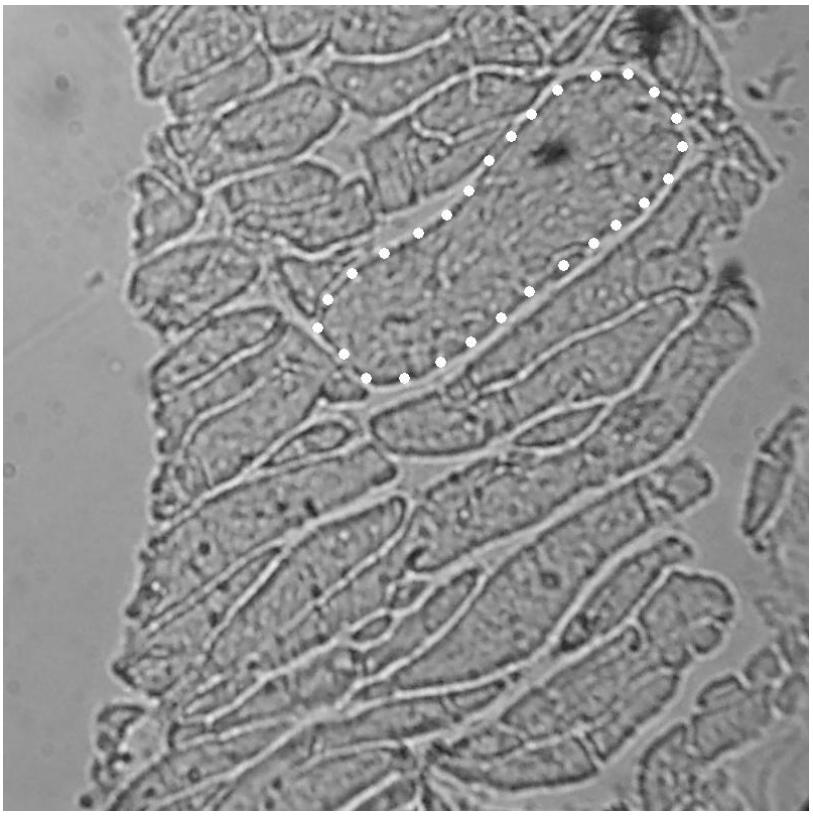

Figure 21: ROI showing outline of sheet used to compare images. The sheet angle for the myolamina outlined by the white dots was found from this image (raw HH ROI) image and the processed image to show that the angle results can be obtained from the raw images and the image processing is not necessary. Note that the data points outlining the sheet are not the actual points taken but are meant only to illustrate which sheet was used.

DISCUSSION

Introduction

In this study, the goal was to develop an imaging method and image processing techniques that would clearly show the microstructure of a rat heart while eliminating the need for some of the harmful chemicals that have been used in previous studies. Investigators often use stains like picrosirius red (PSR) to enhance the contrast between collagen and myocytes. Ingredients in this stain and the fixative used along with it are dangerous to handle because they are irritating, and one in particular, picric acid, is highly explosive (Ricca Chemical Company, 2001; J.T. Baker, 2003). Formalin was used for fixation and JB-4 media was used for embedding. Both formalin and JB-4 are irritants and toxic when ingested, and although they were still used, the need for additional chemicals for staining was eliminated. These methods were first attempted on solid blocks of unstained tissue, but conclusive results were not obtained. However, the myolaminate structure was clearly visible on unstained sections of tissue and the collagen signal was enhanced through image processing techniques. This method was more efficient and simpler than the current methods being used to examine the laminar microstructure of the heart.

Discussion of Image Processing Techniques

For this system, camera gain had to be accounted for because the camera adjusted the gain for each polarization image. For instance, when the polarizers were crossed, the minimum amount of light was transmitted, but the camera increased the gain so as to let in more light. The camera gain was calculated directly from Equation 6 when the polarizer and analyzer were aligned parallel or offset by 45º. When the polarizer and analyzer were crossed, however, this equation could not be used because there was never complete extinction (i.e. $I_{BG\_(400,400)}$ was never truly zero). If this equation had been used, some number would have been divided by zero. To find the camera gain when the polarizer and analyzer were crossed, a black region around the

field of view (extra-ocular region) for each image was observed. Theoretically, this black should be the same intensity for each image; however, the camera adjusted the gain for each image resulting in varying degrees of darkness in the extra-ocular region. The extra-ocular blackness in each image was compared to the brightest extra-ocular blackness of a non-crossed image using a ratio in which the only unknown was the camera gain for the image of interest. For these data, the image with the brightest extra-ocular blackness was VP because the camera gain was the highest. By dividing each image by the calculated camera gain, the effects of a differential gain were removed and all images had the same gain as the HH image. A matrix of scalars representing the background intensity at node 4 for each image was obtained by dividing the intensity of each background image at node 4 by the corresponding camera gain. These background intensity values were subtracted from the images adjusted to account for background and camera gain, resulting in a difference matrix. The magnitude of this difference matrix represents how the sample differs from the background at each pixel location. The image of this magnitude did in fact show enhanced contrast between the collagen and the myocytes. The edges of the myolaminae are bordered by collagen, which appears brighter than the myocytes. Another way of describing this is to say that the collagen differs from the background more than the myocytes do. These image processing techniques enhanced this greater difference, thus making the collagen appear even brighter. The final image that resulted from the image registration process was blurry in comparison to the raw images. This is most likely due to a slight change in the registration of the images that may have occurred each time the camera button was pressed to capture a raw image.

The ultimate goal for the imaging methods developed in this thesis is to enable future investigators to clearly see and quantify the laminar microstructure of the heart. With these quantitative two-dimensional data, researchers can develop a three-dimensional model of the microstructure. Preliminary fiber angles and sheet angles were put into a custom code developed by Dr. John Criscione that illustrates the myolaminate morphology (Jetton, 2004). Figure 22 shows the model that resulted from these data.

Red lines indicate the fiber angle for each slice while the green surface represents the sheet angle for each slice. The model assumes only one family of sheets, but future research will be based on data that are directly observed.

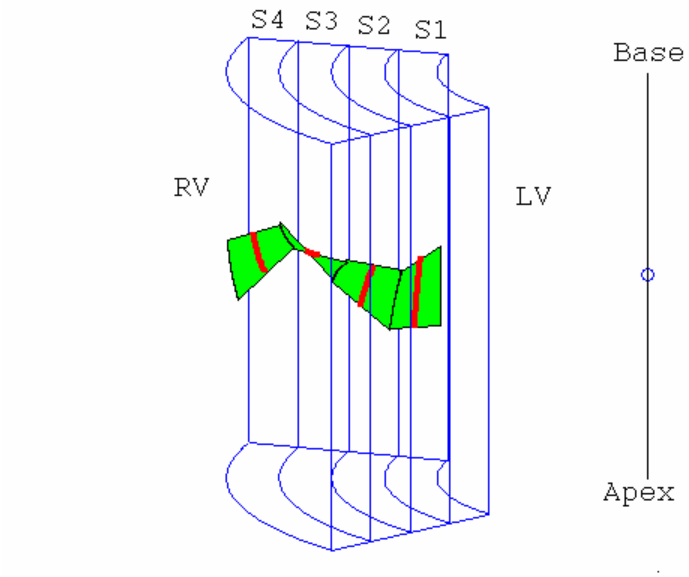

Figure 22: Three-dimensional model of myolaminate morphology. Slices are labeled S1 through S4. The red line represents the fiber angle for each slice and the green surface represents the sheet angle. This model assumes there is only one family of myolaminae, but future research will be directed towards describing the morphology that is directly observed.

Optical Clearing

The contrast between the collagen and myocytes was not enhanced by the image processing methods as much as expected. This may have been due to optical clearing of the tissue. Optical clearing is believed to be the result of a loss of organization and dissociation of collagen fibers within tissue (Yeh et al., 2003). JB-4 embedding media

causes the tissue to become somewhat transparent, indicating that the structure is not maintained. The birefringence of collagen was fundamental to these methods, but the collagen signal was degraded. Typically, when polarizers are crossed, collagen appears bright white on a dark background as a result of its birefringence, but this was not observed. For example and illustration, paper is highly birefringent due to the presence of fibers (i.e. it possesses form birefringence) and the fibers in the paper backing that was placed on the samples did appear bright white in the crossed polarization images. Figure 23 is the raw image of the PM polarization combination. The paper is highly visible at the far right of the field of view due to its birefringence. The polarizers are crossed, meaning the minimal amount of light is being transmitted, but the paper rotates the polarized light, allowing it to pass through. The paper is visible in all of the crossed polarization images. Therefore, it can be concluded that the system is capable of showing striking contrast due to birefringence. It is believed that an embedding media that stabilizes the collagen structure should result in a much higher collagen signal and thus greater contrast between the myocytes and the ECM. However, even with the collagen degradation, the myolaminae and the gaps present between them could be seen without the enhanced contrast that was expected. If an embedding media that did not clear the tissue were to be used in the future, this image processing method may offer improved contrast enhancement.

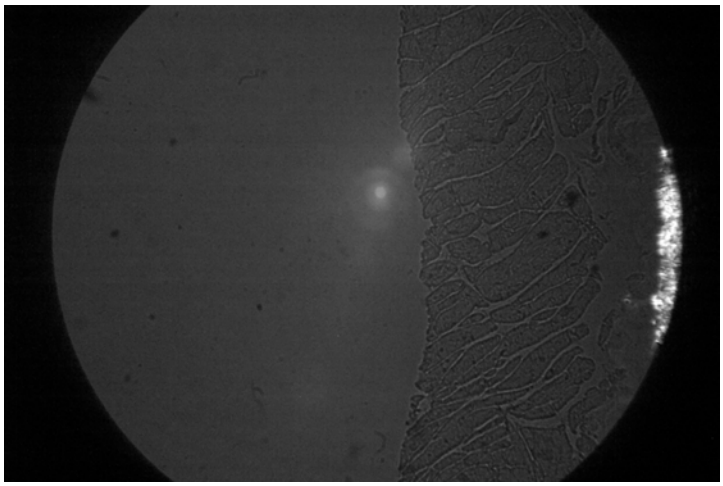

Figure 23: Raw crossed polarization image showing the birefringent paper backing. The paper appears bright on a dark background due to its birefringence. The collagen, however, is not visible suggesting that the embedding media cleared the tissue thus degrading the collagen signal.

CONCLUSIONS AND RECOMMENDATIONS

The goal in this research was to develop an efficient method by which the cardiac microstructure of rats could be investigated. By developing a method applicable to unstained tissue, the use of harmful chemicals was lessened and the sample preparation process was simplified. Viewing slices of unstained myocardium with polarization microscopy enabled the myolaminae and the gaps present between them to be seen clearly. The orientation of the sheets was clearly visible and quantifiable.

Through image processing techniques, the intensity variation on the images was reduced and the variable gain of the camera was accounted for. The contrast between the collagen and myocytes was further enhanced by comparing how they differed from the background of the image. This enhanced image verified the structure that was visible in the raw polarization images. Although the contrast was enhanced, this enhancement was not as remarkable as expected. The embedding media that was used may have altered the organization of the collagen, resulting in a degraded collagen signal. With different embedding media, one that stabilized the collagen structure, the enhanced contrast could be much more noticeable and useful.

For future investigations of the cardiac microstructure, this method of sample preparation and orientation may be very useful. It will enable researchers to directly measure the sheet angles on sections of unstained tissue. The image processing techniques will allow researchers to take into account the effects that the background and variable camera gain have on an image. Quantitative two-dimensional data can then be used to reconstruct a three-dimensional model of the laminar architecture of myocardium, giving investigators a better understanding of how the heart grows and remodels as it does in health and disease.

REFERENCES

American Heart Association, 2003. Heart Disease and Stroke Statistics — 2004 Update. American Heart Association, Dallas.

Anderson, R.R., 1991. Polarized light examination and photography of the skin. Archives of Dermatology 127, 1000-1005.

Arimoto, R., Murray, M., 1996. Orientation-dependent visibility of long thin objects in polarization-based microscopy. Biophysical Journal 70, 2969-2980.

Berne, R.M., Levy, M.N., 2001. Cardiovascular Physiology, 8th Edition. Mosby, St. Louis.

Braunwald, E., 2001. Heart failure. In: Braunwald, E., Fauci, A.S., Kasper, D.L., Hauser, S.L., Longo, D.L., Jameson, J.L. (Eds.), Harrison's Principles of Internal Medicine, 15th Edition. McGraw-Hill, New York, pp.1318-1329.

Caulfield, J.B., Borg, T.K., 1979. The collagen network of the heart. Laboratory Investigation 40, 364-372.

Cleutjens, J.P.M., Verluyten, M.J.A., Smits, J.F.M., Daemen, M.J.A.P., 1995. Collagen remodeling after myocardial infarction in the rat heart. American Journal of Pathology 147, 325-338.

Costa, K.D., May-Newman, K., Farr, D., O'Dell, W.G., McCulloch, A.D., Omens, J.H., 1997. Three-dimensional residual strain in midanterior canine left ventricle. American Journal of Physiology 273, H1968-H1976.

Costa, K.D., Takayama, Y., McCulloch, A.D., Covell, J.W., 1999. Laminar fiber architecture and three-dimensional systolic mechanics in canine ventricular myocardium. American Journal of Physiology 276, H595-H607.

Demos, S.G., Alfano, R.R., 1997. Optical polarization imaging. Applied Optics 36, 150-155.

Emery, J.L., Omens, J.H., 1997. Mechanical regulation of myocardial growth during volume-overload hypertrophy in the rat. American Journal of Physiology 273, H1198-H1204.

Feldman, A.M., Weinberg, E.O., Ray, P.E., Lorell, B.H., 1993. Selective changes in cardiac gene expression during compensated hypertrophy and the transition to cardiac decompensation in rats with chronic aortic banding. Circulation Research 73, 184-192.

Humphrey, J.D., 2002. Cardiovascular Solid Mechanics. Springer, New York.

Inoko, M., Kihara, Y., Morii, I., Fujiwara, H., Sasayama, S., 1994. Transition from compensatory hypertrophy to dilated, failing left ventricles in Dahl salt-sensitive rats. American Journal of Physiology 267, H2471-H2482.

J.T. Baker, 2003. Material Safety Data Sheet: Picric acid. Mallinckrodt Baker, Inc., Phillipsburg, New Jersey.

Jacques, S.L., Roman, J.R., Lee, K., 2000. Imaging superficial tissues with polarized light. Lasers in Surgery and Medicine 26, 119-129.

Jacques, S.L., Ramella-Roman, J.C., Lee, K., 2002. Imaging skin pathology with polarized light. Journal of Biomedical Optics 7, 329-340.

Jetton, E.J., 2004. The Development of Processing Methods for a Quantitative Histological Investigation of Rat Hearts. M.S. Thesis, Texas A&M University, College Station.

Jouk, P.S., Usson, Y., Michalowicz, G., Parazza, F., 1995. Mapping of the orientation of myocardial cells by means of polarized light and confocal scanning laser microscopy. Microscopy Research and Technique 30, 480-490.

Junqueira, L.C.U., Bignolas, G., Brentani, R.R., 1979. Picrosirius staining plus polarization microscopy, a specific method for collagen detection in tissue sections. Histochemical Journal 11, 447-455.

Kenchaiah, S., Pfeffer, M.A., 2004. Cardiac remodeling in systemic hypertension. The Medical Clinics of North America 88, 115-130.

LeGrice, I.J., Smaill, B.H., Chai, L.Z., Edgar, S.G., Gavin, J.B., Hunter, P.J., 1995a. Laminar structure of the heart: ventricular myocyte arrangement and connective tissue architecture in the dog. American Journal of Physiology 269, H571-H582.

LeGrice, I.J., Takayama, Y., Holmes, J.W., Covell, J.W., 1995b. Impaired subendocardial function in tachycardia-induced cardiac failure. American Journal of Physiology 268, H1788-H1794.

Oldenbourg, R., Salmon, E.D., Tran, P.T., 1998. Birefringence of single and bundled microtubules. Biophysical Journal 74, 645-654.

Omens, J.H., 1998. Stress and strain as regulators of myocardial growth. Progress in Biophysics & Molecular Biology 69, 559-572.

Pantic-Tanner, Z., Eden, D., 1999. Calculation of protein form birefringence using the finite element method. Biophysical Journal 76, 2943-2950.

Paul, S., 2003. Ventricular remodeling. Critical Care Nursing Clinics of North America 15, 407-411.

Pedrotti, F.L., Pedrotti, L.S., 1993. Introduction to Optics, 2nd Edition. Prentice-Hall, Upper Saddle River, New Jersey.

Ricca Chemical Company, 2001. Material Safety Data Sheet: Bouin's fixative solution. Ricca Chemical Company, Arlington, Texas.

Robinson T.F., Cohen-Gould, L., Factor, S.M., 1983. Skeletal framework of mammalian heart muscle. Laboratory Investigation 49, 482-498.

Schoen, F.J., 1999. Heart Failure. In: Cotran, R.S., Kumar, V., Collins, T. (Eds.), Robbins Pathologic Basis of Disease, 6th Edition. W.B. Saunders Company, Philadelphia, pp. 546-550

Streeter, D.D. Jr., 1979. Gross morphology and fiber geometry of the heart. In: Berne, R.M. (Ed.), Handbook of Physiology: The Cardiovascular System. American Physiological Society, Bethesda, Maryland, pp. 61-112.

Tower, T.T., Tranquillo, R.T., 2001. Alignment maps of tissues: II. Fast harmonic analysis for imaging. Biophysical Journal 81, 2964-2971.

Weber, K.T., Sun, Y., Tyagi, S.C., Cleutjens, J.P.M., 1994. Collagen network of the myocardium: function, structural remodeling and regulatory mechanisms. Journal of Molecular and Cellular Cardiology 26, 279-292.

Whittaker, P., Boughner, D.R., Kloner, R.A., 1989. Analysis of healing after myocardial infarction using polarized light microscopy. American Journal of Pathology 134, 879-893.

Whittaker, P., Kloner, R.A., Boughner, D.R., Pickering, J.G., 1994. Quantitative assessment of myocardial collagen with picrosirius red staining and circularly polarized light. Basic Research in Cardiology 89, 397-410.

Wolman, M., 1975. Polarized light microscopy as a tool of diagnostic pathology. Journal of Histochemistry and Cytochemistry 23, 21-50.

Yang, F., Liu, Y.H., Yang, X.P., Xu, J., Kapke, A., Carretero, O.A., 2002. Myocardial infarction and cardiac remodelling in mice. Experimental Physiology 87, 547-555.

Yeh, A.T., Choi, B., Nelson, J.S., Tromberg, B.J., 2003. Reversible dissociation of collagen in tissues. Journal of Investigative Dermatology 121, 1332-1335.

Young, A.A., LeGrice, I.J., Young, M.A., Smaill, B.H., 1998. Extended confocal microscopy of myocardial laminae and collagen network. Journal of Microscopy 192, 139-150.

VITA

Kristen Kay Hudson was born in Arlington, Texas in May of 1980. After moving around as a child, her family settled in Westlake Village, California where she completed high school in 1998. She chose to attend Texas A&M University to obtain a Bachelor of Science degree in biomedical engineering, which she received in December of 2002. During her time as an undergraduate, she worked in the Comparative Dermatopathology laboratory in the College of Veterinary Medicine and participated in the Undergraduate Summer Research program where she was first introduced to research in cardiac mechanics. Kristen continued her education in biomedical engineering at Texas A&M, earning a Master of Science degree in August of 2004. After school, she plans on moving to the Houston area to pursue a career at NASA as a flight controller. Any future correspondence can be directed to Kristen at the address below.

Kristen Kay Hudson
1210 Camino Village Dr. #3802
Houston, TX 77058